PROCEEDINGS, Thirty-First Workshop on Geothermal Reservoir Engineering
Stanford University, Stanford, California, January 30-February 1, 2006
SGP-TR-179

STRESS AND FAULTING IN THE COSO GEOTHERMAL FIELD: UPDATE AND RECENT RESULTS FROM THE EAST FLANK AND COSO WASH

Nicholas C. Davatzes and Stephen H. Hickman

Earthquake Hazards Team
U.S. Geological Survey Short address
Menlo Park, CA 94025
e-mail: ndavatzes@usgs.gov

ABSTRACT

We integrate new geologic mapping and measurements of stress orientations and magnitudes from wells 34-9RD2 and 58A-10 with existing data sets to refine a geomechanical model for the Coso geothermal field. Vertically averaged stress orientations across the field are fairly uniform and are consistent with focal mechanism inversions of earthquake clusters for stress and incremental strain. Active faults trending NNW-SSE to NNE-SSW are well oriented for normal slip in the current stress field, where the mean S_{hmin} orientation is 108° ± 24° in a transitional strike-slip to normal faulting stress regime. These structures bound regions of intense micro-seismicity and are complexly associated with surface hydrothermal activity. WNW-ESE trending faults are also associated with distinct regions of enhanced seismicity but are only associated with surface hydrothermal activity where they intersect more northerly trending normal faults. These faults show no evidence for Quaternary slip at the surface and are poorly oriented in the modern stress field. These results together with stress magnitudes measured in the East Flank of the field suggest that the most productive portions of the Coso geothermal field are in stress environments conducive to normal faulting. In addition, significant horizontal principal stress rotations are recorded by drilling-induced structures in borehole image logs. These variations in the azimuth of induced structures suggest local stress heterogeneity induced by active fault slip and are consistent with the high rates of seismicity observed in the geothermal field.

This geomechanical model provides a first step in studying the mechanical interactions and permeability of fault zones, their natural evolution, and their response to engineered stimulation. In addition, this model is a critical element of the stimulation strategy that will be applied to Enhanced Geothermal Systems (EGS) well 46A-19RD in the southwest portion of the geothermal field in 2006.

1. INTRODUCTION

Fluid flow in low porosity crystalline rock is largely controlled by connected networks of faults and fractures within the rock mass. However, the permeability of these fracture networks is degraded by alteration and mineral precipitation that accompanies fluid flux across changing temperature, pressure, and chemical gradients. In natural systems, recurrent brittle deformation and frictional failure can regenerate permeability lost to these processes through dilation accompanying slip on rough fracture surfaces, brecciation, and the formation of new fractures. Mismatch between fracture surfaces and rotation of breccia clasts create connected porosity that persists after a slip event. In tectonically active geothermal systems, these mechanisms can be intentionally activated by increasing the fluid pressure at depth to induce shear failure and create new permeability in formerly inaccessible hot rocks. By exploiting existing networks of fractures, we hope to maximize the lateral extent, surface area, and depth of the stimulated fracture network to most efficiently mine heat from the subsurface.

The Coso geothermal field (CGF) is a prime candidate for creating such an Enhanced Geothermal System (EGS). The geothermal field is rooted in highly fractured granitoid rocks that display temperatures greater than ~640°F at depths less than 10000 ft. Permeability is variable and several hot regions currently display extremely low permeability. However, high rates of seismicity in the field demonstrate that it is highly stressed and susceptible to stimulation by shear failure. In this study, we assemble a geomechanical model that includes the geometry of the fault system and the stress state driving deformation in the Coso geothermal field. This model provides a necessary first step in creating a viable and successful stimulation strategy for the new EGS well 46A-19RD, and key information necessary to transfer successful elements of the strategy to other locations.

2. GEOLOGIC SETTING

The Coso geothermal field is located along the western edge of the Eastern California Shear Zone, subjected to both strike-slip and normal faulting. The field is situated in diorite, quartz diorite, granodiorite, and minor basalt above a shallow heat source presumed to be a partially molten magma body at depths as shallow as 4-5 km (Wicks *et al*., 2001; Monastero *et al*., 2005). At the surface, intrusion of the magma body has resulted in Pliocene to recent rhyolites domes and basalt flows (Duffield et al., 1980) (Figure 1a). Unruh *et al*. (2002) and Monastero *et al* (2005) suggest that Coso lies within the right (releasing) step between the right lateral Little Lake fault zone to the SW and the Wild Horse Mesa fault to the NE which are associated with strike-slip focal mechanisms. This zone accommodates 6.5±0.7 mm/year dextral shearing (McCluskey *et al*., 2001; Monastero *et al*., 2005).

3. THE FAULT SYSTEM

In this section we attempt to integrate existing fault maps and observations with our own field observations within the active geothermal field to define the fault geometry. However, for brevity we do not present an exhaustive discussion of the rich data set available nor do we discuss conditions at the boundary of the geothermal field. In addition, the full three-dimensional geometry of these faults and their mechanical relationships are subjects of on-going research.

Faults within the CGF can be broken into two distinct groups based on their geometry and inferred style of faulting. One group consists of WNW trending and minor NE trending faults. Many of these faults extend well outside the field and form prominent lineaments. These faults are interpreted as dextral and sinistral strike-slip faults respectively by Duffield *et al*. (1980) and Roquemore (1984). Activity on these faults is not entirely clear at this time. They are exposed most often in bedrock and do not clearly offset any Quaternary sediment, but are associated with diffuse micro-seismicity in the geothermal field and with some minor geomorphic expression. The relationship of the diffuse cloud of seismicity to the faults is difficult to interpret at this time, but this problem may be solved by the efforts of the Navy Geothermal Program Office and the U.S. Geological Survey to more accurately relocate these earthquakes. At this time, we interpret these faults to be relatively inactive.

The other group consists of normal faults that dominantly trend N to NNE and dip both west and east (Figure 1a). The most prominent of these fault systems is the Coso Wash normal fault which coincides with the eastern margin of the geothermal field. It is composed of several *en-echelon* NNE-SSW trending segments variably connected by NW-trending, probably oblique-slip, faults. Normal faults appear to have been active in the Quaternary based on geomorphic expression (Angela Jayko, pers. comm. 2004), offset hydrothermal deposits (Hulen, 1978), and offset basalt flow (Figure 1a). A subset of this normal fault population also offsets Holocene basin sediments (Unruh and Streig, 2004), creates local sediment catchments, and is associated with seismicity. Thus, we interpret these faults to be actively slipping.

The normal faults divide the geothermal field into three main geologic sub-regions (Figure 1a): the Main Field, a central spine of exposed bedrock which includes the East Flank region, and Coso Wash. The Main Field is associated with high seismicity rates, high temperatures (>640ºF at <10,000 ft depth), and Quaternary rhyolite domes (Bishop and Bird, 1987). The spine of exposed bedrock extends north to south. Its intensely normal faulted eastern margin hosts the East Flank reservoir. With the exception of the East Flank region which is associated with high temperatures and seismicity, the central region is largely aseismic and cool (Lutz *et al*., 1996). The East Flank also stands out from the rest of this area because of the high normal fault density roughly located on the footwall side of a step between two Coso Wash normal fault segments. Coso Wash is a series of sub-basins associated with segments of the Coso Wash fault and experiences the least seismicity and low temperatures (Davatzes and Hickman, 2005b). The intersection of the N to NNE normal faults with the WNW faults dissects all three regions of the geothermal field into rhombohedral fault-bounded blocks.

4. STRESS MEASUREMENTS

Details of the stress state that these faults are subjected to have been revealed through the analysis of borehole image data and hydraulic fracturing stress measurements (Geomechanics International, 2003; Sheridan and Hickman, 2004; Davatzes and Hickman, 2005) and inversion of focal mechanism data for the principal stress axes (Feng and Lees, 1998) and incremental strain axes (Unruh *et al*., 2002). In this section, we reanalyze some of these earlier results and present new results and analyses from wells 34-9RD2 and 58A-10.

4.1 Orientation of principal stresses from borehole image logs

Concentration of tectonic stress around the free surface of a borehole induces failure of the rock adjacent to the borehole wall as well as immediately ahead of the drill bit. Field studies have demonstrated that these induced structures reliably record the

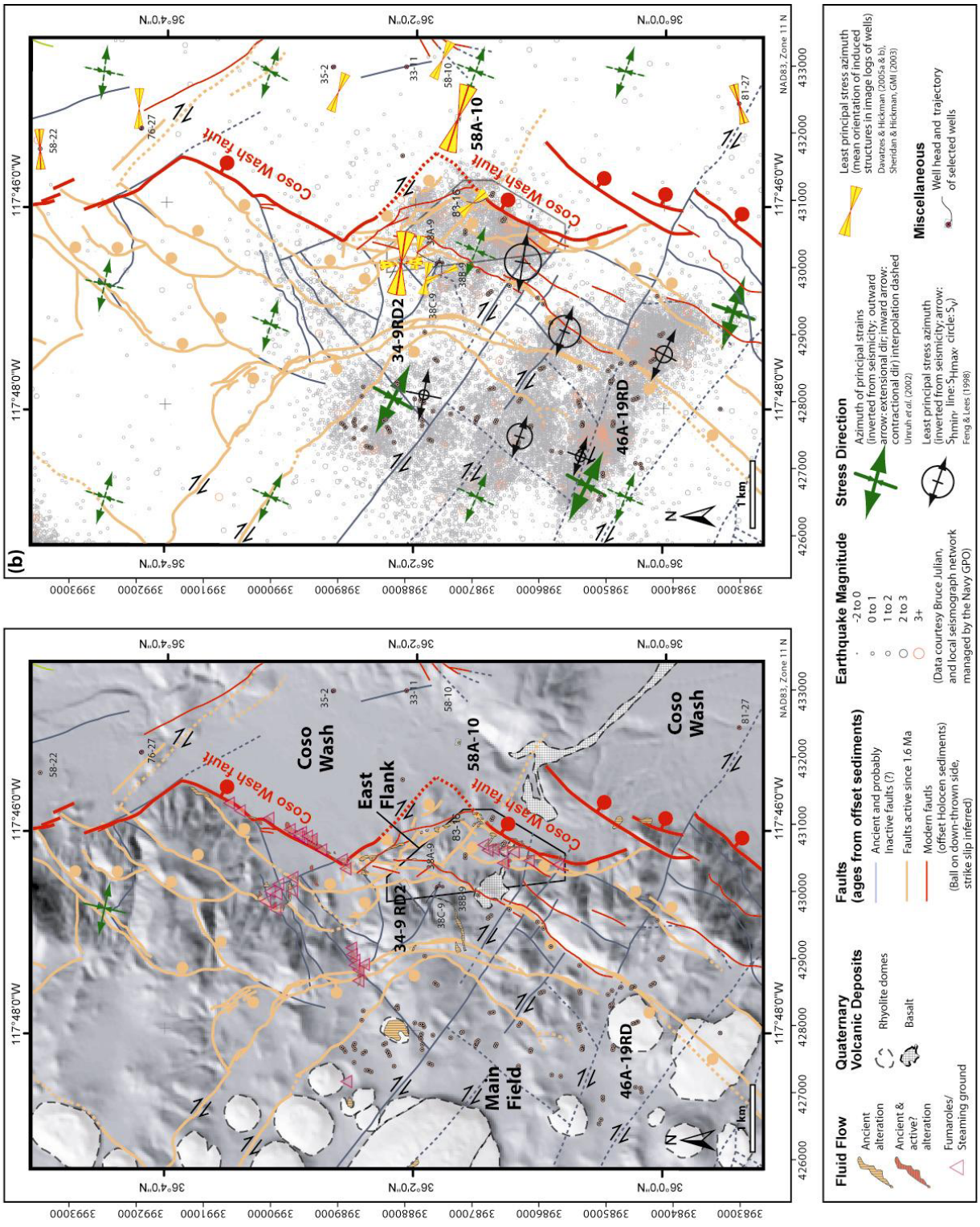

Figure 1: *(a) Tectonic map of the east flank of the Coso geothermal field over shaded relief image of topography. Location of alteration, fumaroles, and steaming ground is based on new mapping and results from Hulen (1978), Duffield et al. (1980), Whitmarsh (1998), Jayko (Personal communication, 2004), and work by Unruh and Streig (2004). (b) Minimum horizontal stress orientations inferred from borehole image logs from Geomechanics International (2003), Sheridan et al. (2003), Sheridan and Hickman (2004) and Davatzes and Hickman (2005a). Wells discussed in this paper are indicated, as are stresses and incremental strains inferred from clusters of seismicity from 1980 to 1995 (Feng and Lees, 1998) and 1980 to 1998 (Unruh et al., 2002). Both analysis combine data from the Southern California Seismic Network with the local seismic array at Coso maintained by the Navy Geothermal Program office.*

orientations of the horizontal principal stress axes (see Moos and Zoback, 1990; Zoback *et al.*, 2003; Davatzes and Hickman, 2005). Three types of drilling-induce structures are recognized: (1) breakouts, (2) tensile fractures and (3) petal-centerline fractures (see Davatzes and Hickman, 2005a for details). Breakouts are patches of the borehole wall that undergo compressive failure and occur in pairs oriented along the minimum horizontal principal stress (S_{hmin}) azimuth (Figure 2a). In contrast, tensile failure of the borehole wall or ahead of the drill bit produces pairs of tensile fractures (Figure 2a) and petal-centerline fractures (Figure 2b) respectively that strike along the maximum horizontal principal stress (S_{Hmax}). These structures can be identified and their azimuthal orientations measured from oriented images of the borehole wall reflectivity, microresistivity and radius, providing a means to infer the direction of the horizontal principal stress axes. In the CGF, image logs have been obtained with the ABI85 High Temperature Borehole Televiewer (ABI85), Formation Micro Imager (FMI), Hot Hole Formation Micro Scanner (FMS), and Electrical Micro-Imager (EMI) in the East Flank and Coso Wash areas.

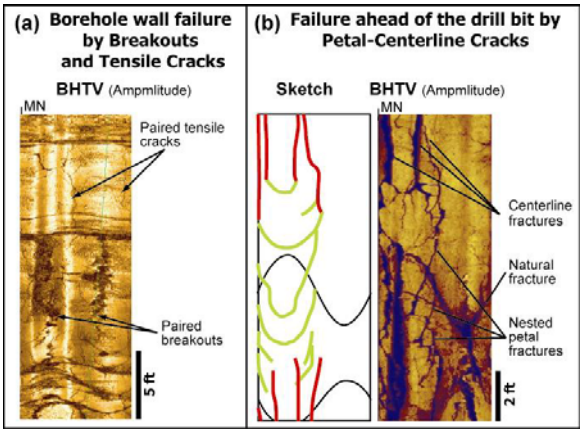

Figure 2: *Drilling-induced structures visible in borehole image logs indicating the modern orientation of the principal horizontal stresses. (a) ABI85 amplitude image of breakouts appear as paired irregularly shaped patches 180º apart and offset 90º from tensile fractures, which appear as paired borehole axis-parallel or en echelon lineations 180° apart. (b) In the ABI85 amplitude image of petal fractures appear as smoothly curving chevrons. The arms of the chevrons merge with pairs of centerline fractures oriented parallel to the borehole axis, but with variable azimuthal separation. Note that the borehole images are un-wrapped from a full 360° view, thus planar structures intersecting the borehole appear as sinusoids.*

These logs were checked against borehole deviation surveys and other overlapping image logs to verify accurate image orientations. Borehole deviation over the interpreted intervals range from 3º to 15º which allowed us to neglect corrections required for highly deviated boreholes (Peska and Zoback, 1995). Following the method of Davatzes and Hickman (2005a) the orientation of S_{hmin} was determined from the average of pairs of petal-centerline fractures or tensile cracks. Thus, tensile fractures of either kind were only picked when they occurred as pairs. Mean orientations of S_{hmin} are calculated by averaging the orientation of induced structures weighted by their cumulative lengths. Each type of structure was given equal value in this analysis.

New results from wells in the East Flank and Coso Wash

New analyses of image logs acquired in 34-9RD2 and 58A-10 reveal extensive suites of drilling-induced petal-centerline fractures, tensile borehole wall fractures, and to a lesser extent borehole wall breakouts. No breakouts were observed in the East Flank well 34-9RD2 (Figure 3), which is similar to the analysis of nearby well 38C-9 in which only one breakout was seen (Sheridan and Hickman, 2004). However abundant tensile fractures and petal centerline fractures indicate that the azimuth of S_{hmin} in proximity to the well is bimodal (Figure 3a). The dominant mode is 099º ± 18º, and a subsidiary mode with limited vertical extent is 176º ± 15º (Figure 3b). In Coso Wash well 58A-10, breakouts are more prevalent but are narrow and shallow. Overall, they represent a small percentage of the total length of induced structures. Near well 58A-10, S_{hmin} is oriented along an azimuth of 108º ± 15º (Figure 4a).

4.2 EAST FLANK STRESS MAGNITUDES

We used a variety of techniques to determine the magnitude of S_{hmin} and S_{Hmax} in the East Flank. The magnitude of S_{hmin} was determined from a hydraulic fracturing stress test conducted previously in well 38C-9 (Sheridan and Hickman, 2004) and a new test conducted in well 34-9RD2 in February 2005 (presented here for the first time). In addition, upper bounds on the magnitudes of S_{Hmax} were obtained through borehole failure analyses based upon the presence or absence of breakouts in wells 34-9RD2, 38C-9, and 58A-10 (well locations in Figure 1).

Hydraulic Fracturing Stress Measurement in Well 34-9RD2

As done in other geothermal wells (see Hickman et al., 1998; Sheridan and Hickman, 2004), following cementation of the casing at a depth of 7903 ft measured depth (MD), a 79-foot-long pilot hole was drilled out the bottom of the well in which to conduct the hydraulic fracturing test. A drill-pipe-deployed

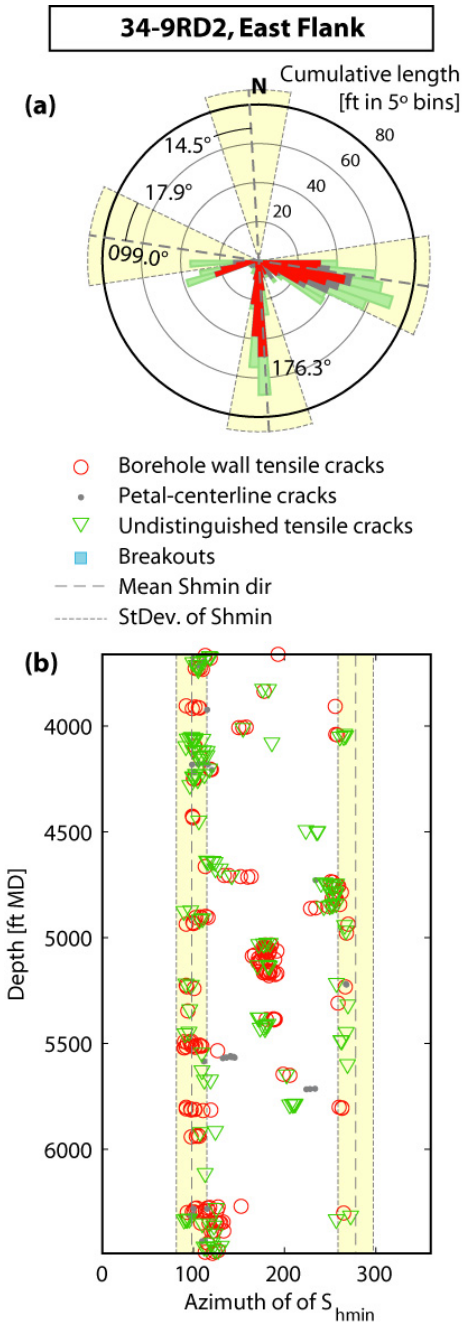

Figure 3: *(a) Rose diagram of induced structure orientations weighted by structure length in 5° bins. (b) Depth distribution and orientations of S_{hmin} inferred from drilling-induced structures in well 34-9RD2 (location in Figure 1). Depth units are measured depth (MD).Some tensile cracks could not be distinguished between petal centerline cracks and borehole wall tensile fractures and are correspondingly marked.*

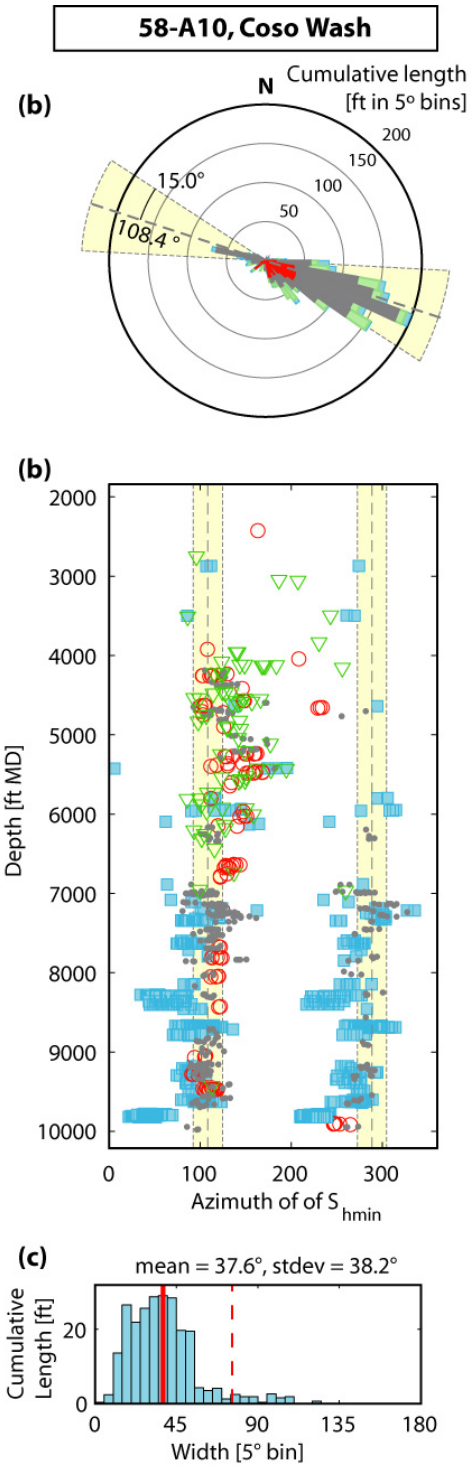

Figure 4: *(a) Rose diagram of induced structure orientations weighted by structure length in 5° bins. (b) Depth distribution and orientations of S_{hmin} inferred from drilling-induced structures in well 58A-10 (location in Figure 1; Legend in Figure 3). (c) Cumulative length of breakouts of different width.*

packer (RTTS tool) was then set in the cased hole at a depth of 7869 ft MD and the pipe was pressurized to induce a hydraulic fracture in the uncased pilot hole. Repeated pressurization cycles were then employed to extend this fracture away from the borehole (Figure 5a). Pressures and flow rates were measured at the surface and extrapolated to depth using a fluid pressure profile determined immediately before the hydraulic fracturing in conjunction with a high-accuracy, temperature-compensated quartz pressure gauge run inside the drill pipe to a depth of 7479 ft MD. This gauge encountered a restriction in the pipe internal diameter at this depth and had to be removed before the test could begin.

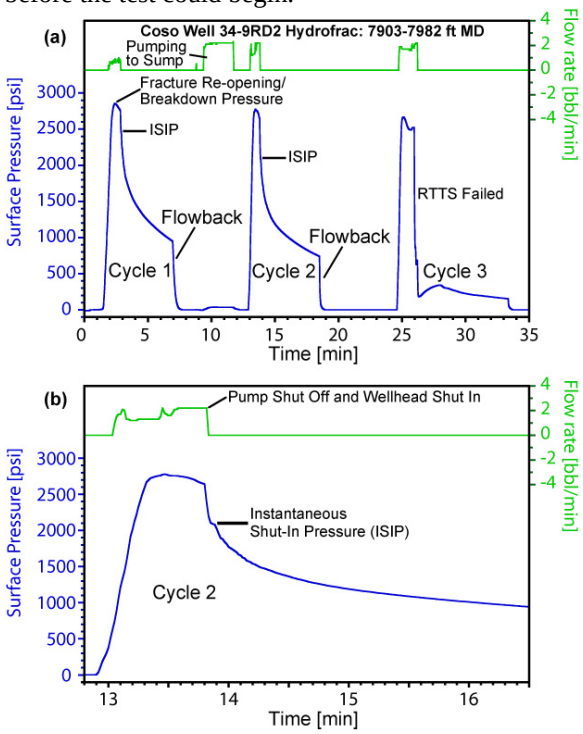

Figure 5: *(a) Surface pressure and flow-rate records from the hydraulic fracturing stress measurement conducted in well 34-9RD2 at a measured depth (MD) of 7903-7982 ft. For the first two cycles, fluid was pumped into the well at flow rates of 1-2 barrels/min for about 1 minute, the well was shut in and the pressure monitored for about 5 minutes, and the wellhead was vented to the drill sump (flowback) to drain the hydraulic fracture prior to the next cycle. This test was terminated prematurely after the RTTS packer failed in the middle of the third cycle. Fluid was pumped to the drill sump (bypassing the well) between cycles 1 and 2 in an unsuccessful attempt to reactivate a malfunctioning flow meter. (b) Expanded view of cycle 2 from this test, showing how the instantaneous shut-in pressure (ISIP, also shown in Figure 5a) was determined. Note how the pressure flattens out and then drops slightly during pumping, indicating that the hydraulic fracture has reopened and is propagating away from the borehole prior to shut in.*

Following Hickman and Zoback (1983), the magnitude of S_{hmin} was determined from the instantaneous shut-in pressure (ISIP), or the pressure at which the pressure-time curve departs from an initial linear pressure drop immediately after the pump is turned off and the well is shut in (Figure 5b). Although we typically run a hydraulic fracturing test for multiple cycles to check for repeatability of the ISIP, the RTTS tool failed in the middle of the third cycle, allowing fluid to bypass the packer and flow out the top of the casing. However, the ISIP determined from the second cycle was very distinct (Figure 5b) and the observation that the pumping pressure in cycle 3 just before the RTTS tool failed had leveled out at close to the value attained in cycle 2 suggests that viscous pressure losses within the hydraulic fracture near the borehole were very small and that the ISIP from the second cycle is a good measure of S_{hmin} (see discussion of the relation between pumping pressure and ISIP in Hickman and Zoback [1983] and Hickman et al. [1988]). Thus, using directional surveys to convert from MD to total vertical depth below ground level (TVD), our analysis of the hydraulic fracturing data from well 34-9RD2 shows that the magnitude of S_{hmin} at 7817 feet TVD is 5635 ± 200 psi (Figure 6).

We calculated the vertical stress (S_V) using a geophysical density log run in well 34-9RD2 at depths of 3609-6497 ft MD and making the reasonable assumption (based upon the uniform lithology penetrated by this well) that the average density from this log (2.65 gm/cm^3) applied throughout the entire well. In accordance with the Coulomb failure criterion, frictional failure (i.e., normal faulting) would then occur at a critical magnitude of S_{hmin} given by (Jaeger and Cook, 1979):

$$S_{hmin\ crit} = (S_V - P_p) / [(\mu^2 + 1)^{1/2} + \mu]^2 + P_p \qquad (1)$$

where μ is the coefficient of friction of preexisting faults. It is assumed here that μ ranges from 0.6 to 1.0, in accord with laboratory sliding experiments on a variety of rock types (Byerlee, 1978). Estimates of undisturbed (i.e., preproduction) formation fluid pressure were obtained assuming that P_p was in hydrostatic equilibrium with a water table at the surface (Paul Spielman, pers. comm.. 2003; Joe Moore, pers. comm. 2004) and by integrating water density as a function of pressure and temperature as appropriate to ambient geothermal conditions, and including a small correction for total dissolved solids. In this manner, we calculated the range of S_{hmin} magnitudes at which normal faulting would be expected along optimally oriented faults (Figure 6).

Bounds on Greatest Horizontal Principal Stress

Borehole breakouts occur where the stress concentration at the borehole wall exceeds the

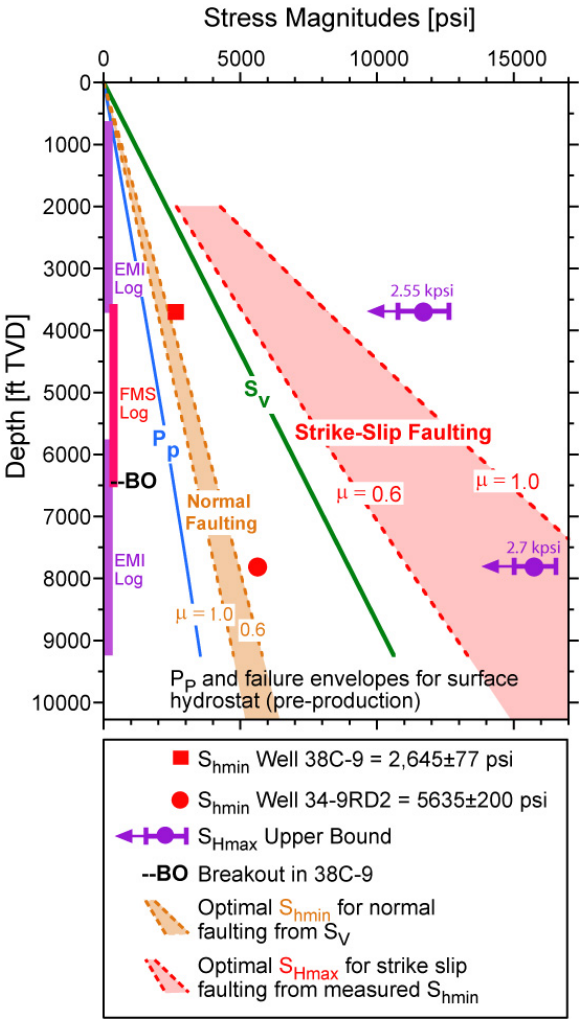

Figure 6: *Stress magnitudes for the East Flank derived from measurements in wells 38C-9 (Sheridan and Hickman, 2004) and 34-9RD2 (locations in Figure 1). The least horizontal principal stress (S_{hmin}) was measured using hydraulic fracturing tests at 3703 ft total vertical depth (TVD) in well 38C-9 (Sheridan and Hickman, 2004) and at 7817 ft TVD in well 34-9RD2 (Figure 5). The depth extent of image logs acquired in the two wells is shown by vertical lines, with the EMI log obtained in 38C-9 and the FMS log obtained in 34-9RD2. The symbol "BO" denotes the sole breakout observed in these two wells, which was seen at a depth of 6419 ft in well 38C-9. Upper bounds (with error bars) to the greatest horizontal principal stress (S_{Hmax}) were obtained based on the general absence of breakouts using the estimates of C_0 shown in Figure 6c. Dashed orange lines indicate the range of S_{hmin} magnitudes at which normal faulting would be expected given the calculated vertical stress (S_v) for coefficients of friction of 0.6–1 (see text). Red dashed lines indicate the range of S_{Hmax} where strike-slip faulting would be expected assuming that S_{hmin} increases linearly with depth and passes through the values of S_{hmin} measured in these two wells. Pore pressure (P_p) and failure envelopes were drawn assuming that the pre-production water table was in hydrostatic equilibrium with the surface under present-day thermal conditions.*

unconfined compressive strength (C_0) of the rock (Moos and Zoback, 1990). Thus, the presence or absence of breakouts and their widths constrain the stress state along the well if C_0 is known. Given that only a single breakout was observed in well 38C-9 (Sheridan and Hickman, 2004) and none were observed in well 34-9RD2 (this study), we used the general absence of breakouts in both wells to determine upper bounds to the magnitude of S_{Hmax}. This analysis used S_{hmin} magnitudes measured in both wells (Figure 6) together with theoretical models for breakout formation in inclined wells based upon the elastic concentration of stresses around a circular borehole (Moos and Zoback, 1990; Peska and Zoback, 1995).

This represents a new analysis for well 34-9RD2 and an update to previous bounds on S_{Hmax} from well 38C-9 (Sheridan and Hickman, 2004) using recent laboratory measurements of rock mechanics parameters carried out under the EGS project (TerraTek, 2004). These measurements were conducted on dry hornblende-biotite-quartz diorite (HBQ diorite) from Coso well 64-16 at approximately 2820 ft MD. The use of these data in our analysis is justified since HBQ diorite best represents rocks encountered in wells 38C-9 and 34-9RD2 (Kovac and Moore, 2005).

To estimate C_0 we used uniaxial and triaxial measurements of compressive strength on HBQ diorite (Figure 7a) to obtain a reference value for C_0. This value, together with laboratory measurements of V_P on the same samples at high confining pressures (TerraTek, 2004), was then compared to measurements of C_0 as a function of V_P from core samples of Lac du Bonnet granite at depths up to 1 km (Annor and Jackson, 1987; Figure 7b). (Annor and Jackson currently provide the most complete and readily available measurements of C_0 and V_P in granitoid rocks acquired by a single high quality method.) We then required that a least squares fit of a straight line to the Annor and Jackson data pass through C_0 determined for the HBQ diorite to arrive at the following empirical strength law for the East Flank:

$$C_0 = 13899.29 + 2358.3(V_P) \qquad (2)$$

where C_0 is in psi and V_P is in km/sec. We then applied Equation 2 to in-situ measurements of V_P from wireline logs to estimate C_0 as a function of

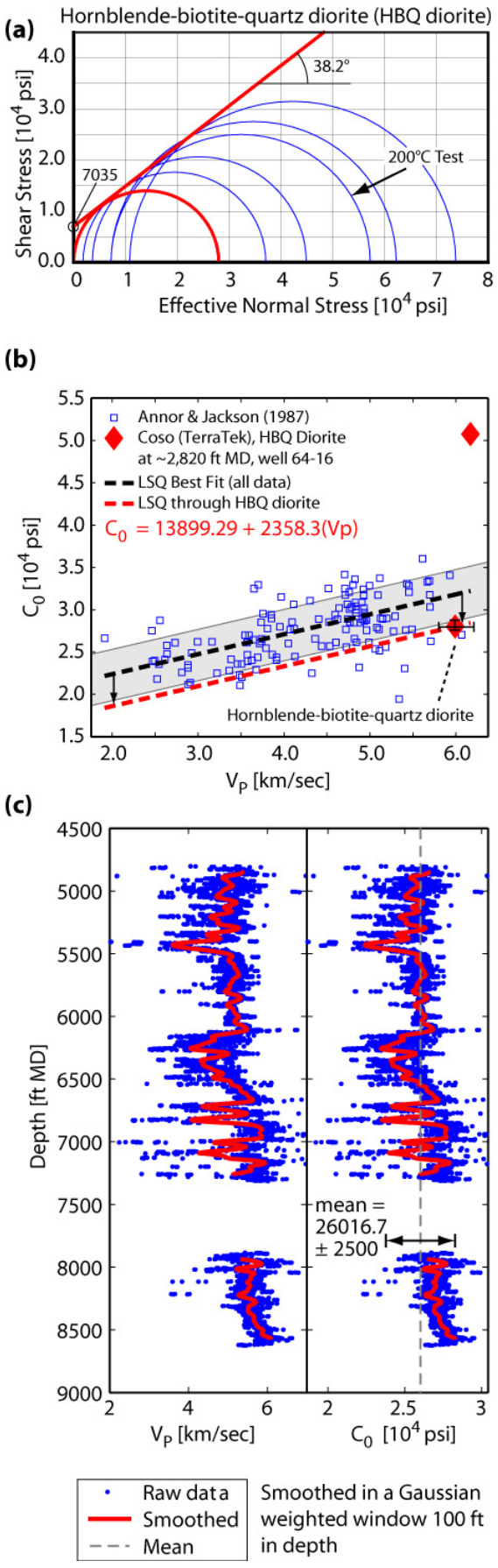

Figure 7: *(a) Mohr diagram showing compressive strengths determined on 6 samples of dry hornblende-biotite-quartz diorite (HBQ diorite) from Coso well 64-16 at approximately 2820 ft MD (TerraTek, 2004). The red circle represents an unconfined compressive strength (C_0) test, whereas the other circles represent triaxial compressive strength tests at a variety of confining pressures. The Mohr-Coulomb failure criterion for this rock (red line tangent to these circles) is very well-constrained, with cohesion of 7035 psi and internal friction angle of 38.2°. Although most tests were conducted at room temperature, one test at 200° C indicates that short-term compressive strength for these rocks is relatively insensitive to temperature. (b) Unconfined compressive strength (C_0) as a function of P-wave velocity (V_P) from tests on Lac du Bonnet granite (Annor and Jackson, 1987) and the Coso HBQ diorite. Linear least squares best fit to the Annor and Jackson data (black dashed line) was forced to coincide with the strength and V_P measurements made on the Coso HBQ diorite (red dashed line, Equation 1 in the text). The overall error due to scatter of the Annor and Jackson data is represented by the grayed region. (c) Raw and smoothed V_P log of well 34-9RD2 and estimated variation of C_0 with depth using Equation 2.*

depth in well 34-9RD2 (Figure 7c). Gaussian smoothing of the V_P data best represents bulk properties of the host rock while giving some estimate of the uncertainty in the measurements and is therefore used to constrain C_0 in the stress model. Estimated values of C_0 range from 18,720 to 30,360 psi in the raw data and 22,490 to 27,910 psi in the smoothed data, probably reflecting variations in rock type and damage as well as hydrothermal alteration along the borehole (Figure 7c) as documented by Kovac *et al.* (2005). Additional uncertainty in this empirical correlation is indicated by the error bars in Figure 7c. As no V_P logs are available for well 38C-9, we used the average strength from the upper part of 34-9RD2 (Figure 7c) to estimate S_{Hmax} for that well. The values of C_0 used to constrain S_{Hmax} in wells 34-9RD2 and 38C-9 were 27,000 psi and 25,500 psi, respectively. These values will be further refined when we carry out rock mechanics tests on core recently recovered from well 34-9RD2.

In addition to C_0 and the magnitude of S_{hmin}, several other parameters must be estimated or measured to carry out constrain S_{Hmax}. Borehole deviation angle and azimuth were determined from directional surveys and the local azimuths of S_{hmin} were determined directly from observations of wellbore failure (Figure 3; Sheridan and Hickman, 2004). Current (i.e., post-production) fluid pressures – as

opposed to pre-production values used in our geologic failure analysis (c.f., Figure 6) – are needed to calculate the concentration of effective stresses around the borehole and were estimated from temperature/pressure surveys conducted in both wells during static (shut in) conditions. Minimum drilling mud pressures experienced by logged intervals of each well prior to image logging were determined from daily drilling reports. Finally, the internal friction angle (38.2°) was determined from the slope of the failure envelope in Figure 7a.

5. DISCUSSION

5.1. Stress and strain in the different regions of the geothermal field and outside the Geothermal Field

We integrated the new data from wells 34-9RD2 and 58A-10 with existing analysis conducted by Geomechanics International (2003) after careful quality checking to investigate the variation of stress orientations in the East Flank and Coso Wash. In general, the mean azimuth of S_{hmin} in wells throughout both areas is ~108° ± 24º (Figure 1b). This orientation is consistent with the N- to NNE-striking normal faults that seismicity and/or geomorphology indicate are currently active (Figure 1a). Inside the East Flank, stress orientations indicate somewhat greater heterogeneity than in Coso Wash. Wells 38A-9, 38C-9, and 34-9RD2 indicate stress orientations more similar to the Coso Wash wells. However, wells 38C-9, 83-16, and the subsidiary mode in 34-9RD2 suggest that S_{hmin} is oriented approximately NNW-SSE (Figure 3).

Detailed examination of variations in borehole failure orientations with depth reveals numerous localized stress rotations, such as the prominent rotations at about 5100 ft measured depth (MD) in well 34-9RD2 (Figure 3b) and at 9700 ft MD in well 58A-10 (Figure 4b). Our preliminary modeling of these local rotations in S_{hmin} (not presented here) suggests that they result from slip on faults, indicating active deformation in the crust of the East Flank and adjacent Coso Wash. The range of rotations up to 70º, suggesting fault slip at a variety of scales consistent with micro-seismicity and the abundant large-aperture faults visible in image logs (Sheridan and Hickman, 2004; Geomechanics International, 2003; Davatzes and Hickman, 2005).

An initial comparison of S_{hmin} values from hydraulic fracturing tests in wells 38C-9 (Sheridan and Hickman, 2004) and 34-9RD2 (this study) with the normal faulting failure envelope (Figure 6) indicates that S_{hmin} in the East Flank at depths of 3,000 to 9,000 ft MD is very close to that required for incipient normal faulting on optimally oriented faults. That such optimally oriented faults do, indeed, exist in the East Flank is indicated by surface mapping of faults at high angle to S_{hmin} that offset Holocene sediments (e.g., Figure 1) and by analysis of borehole image logs from 38C-9 and a number of nearby wells (Sheridan and Hickman, 2004). This conclusion is also consistent with the abundant petal-centerline fractures seen in the East Flank and Coso Wash faults, which are favored in normal faulting environments because of the low mean stress (Li and Schmidt, 1998).

However, an immediate assumption that normal faulting dominates is tempered by the potential influence of S_{Hmax}. Analysis of stress magnitudes indicates that S_{Hmax} in the East Flank at depths of 3,000 to 9,000 ft MD could be significantly in excess of S_V (Figure 6). By applying the same type of frictional failure analysis as was applied for normal faulting (i.e., Equation 1) to strike-slip failure, we see that upper bounds to S_{Hmax} are equal to or greater than the critical values required for frictional failure on optimally oriented strike-slip faults under pre-production fluid pressure conditions (Figure 6). If the actual values of S_{Hmax} are close to these upper bounds, then the East Flank of the CGF is in a transitional stress regime between normal and strike-slip faulting. Nonetheless, in the absence of prevalent breakouts with measurable width our analysis of S_{Hmax} only provides upper bounds—so S_{Hmax} could be much smaller. Thus, the propensity for strike-slip faulting in the East Flank, common in the regions surrounding the geothermal field (Monastero *et al*., 2005), is uncertain, whereas the proximity of the measured S_{hmin} to failure (requiring only a $\mu \approx 0.55$ or lower, see Figure 6) strongly suggests that the stress regime in the East Flank favors normal faulting.

In addition to our borehole analyses, several studies have mapped spatial variations in the local state of stress or incremental strain by inversion of spatially clustered populations of earthquake focal mechanisms (Feng and Lees, 1998; Unruh *et al*., 2002). The orientations of the least principal compressive stress or extension direction predicted by these methods are generally uniform within the geothermal field (Figure 1) and similar to borehole measurements. Due to the low rates of seismicity, results for Coso Wash are not available for comparison with borehole results. However, stress directions indicated by extensive borehole observations in Coso Wash are consistent with extension accommodated by adjacent N- to NNE-striking faults such as the Coso Wash fault segments.

More recent earthquake relocations and incremental strain inversions also map an area of extensional strain located over the southern part of the Main Field and extending east and north into the East Flank (Keith Richards-Dinger, pers. comm. 2005). This interpretation is consistent with both the stress and the strain invariants predicted by the previous studies,

and with local GPS- and InSAR-based surface displacement vectors which indicate subsidence above the Main Field and East Flank (Fialko and Simons 2000; Wicks *et al*., 2001; Unruh *et al*., 2002). Such a strain field favors normal faulting and is characterized by relatively low mean stress, consistent with our observations in the East Flank. This low mean stress is expected to facilitate dilation and increased permeability accompanying fault slip. Thus, the relatively low mean stress predicted by these strain data and inversions for the southern part of the Main Field, where EGS well 46A-19RD is located and where permeability is currently low, is favorable for a successful EGS stimulation. This inferred stress state near 46A-19RD will be tested with a hydraulic fracturing stress measurement and borehole image and other logging planned for 2006.

5.2. Fault Rocks

Fault rock mineralogy and texture provide a further control on the formation and maintenance of fluid flow in the geothermal field (Davatzes and Hickman, 2005b) that is not addressed by the above analysis of fault geometry and stress. Core from East Flank well 64-16 reveals two end-member classes of fault rocks at depth: (1) cataclastic fault rocks with mineralogy similar to the host rock but with increased porosity; (2) well-developed clay-rich fault rocks characterized by extremely small, disconnected pores (Davatzes and Hickman, 2005b). These distinct fault zone mineralogies and textures imply variation in the frictional strength, permeability, and slip-induced dilatancy of fault zones (Lockner and Beeler, 2002) within the Coso geothermal field. Whereas we know these different fault types are developing in the geothermal field (Davatzes and Hickman, 2005b), we currently do not have enough data to adequately describe their three dimensional distribution and thus incorporate their impact into an EGS stimulation strategy.

If the crust in the East Flank is currently critically stressed (Townend and Zoback, 2004), *i.e.*, at incipient shear failure, then at least some faults in these regions have coefficients of friction in the range of 0.3 to 0.55. Such low coefficients of friction are common in clay-rich fault zones, and would be compatible with clays identified in cuttings from well 34-9RD2 (Kovac *et al*., 2005). In addition, if production causes draw-down in this compartment, fault slip would only be possible on weaker and weaker faults, and thus could inhibit permeability regeneration by dilatant shear failure.

5.3. Surface hydrothermal activity

Surface expressions of hydrothermal fluid flow in the CGF include steaming ground, fumaroles, and hydrothermal alteration/deposition (Hulen, 1978; Roquemore, 1981; Adams *et al*., 2000). Earliest surface evidence of geothermal activity in the field is represented by the 307ka travertine deposits (Adams *et al*., 2000), which is offset by segments of the Coso Wash fault. Subsequently, sinter indicating higher temperature hydrothermal activity was deposited at approximately 238ka (Duffield *et al*., 1980l; Echols *et al*., 1986; Hulen, 1987). The current hydrothermal activity has developed within the last 10ka and fumaroles. Reservoir boiling leading to acid alteration distributed along fault traces appears to be modern.

These features are preferentially distributed along major NNE-SSW trending normal faults with clear geomorphic expressions such as retaining ponds and fault scarps in basin fill. Intersections between NNE-SSW trending faults and nearly WNW-ESE trending faults (Figure 1a) also appear to localize intense hydrothermal activity. These circumstances support they hypothesis that fluid flow is largely focused along the most active faults and fractures in the CGF. However, simple analysis of the fault geometry and stress state does not currently account for variations in the distribution of hydrothermal activity. Other variables such as the physical properties of fault rocks (Davatzes and Hickman, 2005b), reservoir engineering practices, and the complex 3D fault geometry and mechanical interactions between nearby faults under the current stress field will be addressed in a future study.

7. CONCLUSIONS

Stress orientations from both borehole data and earthquake focal mechanism inversions suggest a consistent remote horizontal stress orientation where S_{hmin} is ~108° ± 24° throughout the productive geothermal field. A faulting regime that favors normal slip in the East Flank of the field is suggested by hydraulic fracturing stress tests that measure $S_{hmin,}$ constraints on S_{Hmax} from borehole breakouts and rock strength, and Holocene sediments offset by modern basin-bounding normal faults. These measurements are also consistent with inversions of seismicity in the upper 0.5 to 2.5 km of the field, which indicate that the East Flank and southern portion of the Main Field are actively extending. Thus, these results suggest that well 46A-19RD is well situated for EGS stimulation through injection-induced shear failure to enhance permeability in a hot but low permeability portion of the Main Field.

8. ACKNOWLEDGMENTS

Much of the data analyzed was made available through the Navy Geothermal Program Office. Funding for N. Davatzes' salary was provided by a U.S. Geological Survey Mendenhall Fellowship. Funding for new data acquired as part of the

Enhanced Geothermal Systems project was funded by the Department of Energy Geothermal Program.

9. REFERENCES

Adams, M.C., Moore, J.N., Bjornstad, S., and Norman, D.I. (2000), Geologic history of the Coso geothermal field. *Proceedings World Geothermal Congress 2000, Kyushu – Tohoku, Japan, May 28 – June 10, 2000*. p. 2463-2469.

Annor, A. and Jackson, R. (1987), Mechanical, thermal and joint properties of rock samples from the Lac du Bonnet Batholith, Manitoba, in *Geotechnical Studies at Whiteshell Research Area (RA-3)*, edited by T.J. Katsube and J.P. Jume, Div. *Rep. MRL 87-52*, CANMET Min. Res. Lab., Ottowa.

Bishop , B.P. and Bird, D.K. (1987) Variation in sericite compositions from fracture zones within the Coso Hot Springs geothermal system. *Geochimica et Cosmochimica Acta*, **15**, 1245-1256.

Byerlee, J. (1978) Friction of rocks. *Pure and Applied Geophys.*, **116**, 615-626.

Davatzes, N.C. and Hickman, S. (2005a), Comparison of acoustic and electrical image logs from the Coso geothermal field, CA. Proceedings, Thirtieth Workshop on Geothermal Reservoir Engineering, Stanford University, January 31-February 2, 2005. SGP-TR-176, p. 1-11.

Davatzes, N.C. and Hickman, S. (2005b), Controls on Fault-Hosted Fluid Flow: Preliminary Results from the Coso geothermal field, CA, GRC Transactions, 29, 343-348.

Duffield, W.A., Bacon, C.R. and Dalrymple, G.B. (1980), Late Cenozoic volcanism, geochronology, and structure of the Coso Range, Inyo County, California. *J. of Geophys. Research*, **85**(B5), 2381-2404.

Echols, T.J., Hulen, J.B., Moore, J.N. and Crane, G. K. (1986), Surficial alteration and spring deposits of the Wheeler mercury prospect, with initial results from Wheeler Corehole 64-16, Coso geothermal area, California. In: *Transactions - GRC, vol.10*. Geothermal Resources Council, Davis, 175-180.

Feng, Q. and Lees, J.M. (1998), Microseismicity, stress, and fracture in the Coso geothermal field, California. In: *Tectonophysics* (edited by Trifu, C. I. and Fehler, M.) **289**. Elsevier, Amsterdam, 221-238.

Fialko, Y. and Simons, M. (2000), Deformation and seismicity in the Coso geothermal area, Inyo County, California: Observations and modeling using satellite radar interferometry. *J. Geophys. Res.*, 105(B9), 21781-21793.

Geomechanics International (2003), Fracture permeability and *in situ* stress in the Eastern Extension of the Coso Geothermal Reservoir: Kinematic and dynamic studies of the Coso Geothermal and surrounding area. *Report prepared for Geothermal Program Office, Contract Number N68936-01-R-0095*, 75 p.

Hickman, S.H. and Zoback, M.D. (1983) The interpretation of hydraulic fracturing pressure-time data for in-situ stress determination, in *Hydraulic Fracturing Measurements*, edited by M.D. Zoback and B.C. Haimson, National Academy Press, Washington, D.C., 44–54.

Hickman, S., Zoback, M. D. and Healy, J. H. (1988) Continuation of a deep borehole stress measurement profile near the San Andreas Fault, I: Hydraulic fracturing stress measurements at Hi Vista, Mojave Desert, CA. *J. Geophys. Res.*, **93**, 15,183–15,195.

Hickman, S., Zoback, M.D. and Benoit, R. (1998) Tectonic controls on reservoir permeability in the Dixie Valley, Nevada, geothermal field. *Proceedings 23rd Workshop on Geothermal Reservoir Engineering, Stanford, CA, Jan. 26-28*, 291-298.

Hulen, J.B. (1978), Geology and alteration of the Coso geothermal area, Inyo County, California. U. S. Department of Energy: Geothermal Energy.

Jaeger, J.C. and Cook, N. G. W. (1979) Fundamentals of Rock Mechanics (Third Edition). New York, Chapman and Hall, 28–30.

Kulander, B.R., Dean, S.L., and Ward, B.J.Jr., (1990) Fractured Core Analysis: Interpretation, Logging, and Use of Natural and Induced Fractures in Core. American Association of Petroleum Geologists, Tulsa, OK. *AAPG Methods in Exploration Series, No. 8*, 88 p.

Kovac, K.M., Moore, J.N., and Lutz, S.J. (2005) Geological framework of the East Flank, Coso geothermal field: Implications for EGS development. *Proceedings 30th Workshop on Geothermal Reservoir Engineering, Stanford, CA, Jan31-Feb2. SGP-TR-176, 7 p.*

Li, Y. and Schmitt, D.R., (1997) Well-bore bottom stress concentration and induced core fractures. *AAPG Bulletin*, **81**(11), 1909-1925.

Li, Y. and Schmitt, D.R., (1998) Drilling-induced core fractures and in situ stress. *J. Geophys. Res.*, **103**(B3), 5225-5239.

Lockner, D.A. and Beeler, N.M. (2002) Rock failure and earthquakes. International Handbook of Earthquake and Engineering seismology, 81A, p. 505-537.

Lorenz, J.C., Finley, S.J., and Warpinski, N.R., (1990) Significance of coring-induced fractures in Mesaverde core, Northwestern, Colorado. *AAPG Bulletin*, **74**(7), 1017-1029.

Lutz, S.J. Moore, J.N., and Copp, J.F. (1996) Integrated mineralogical and fluid inclusion study of the Coso geothermal system, California.

Proceedings 21st Workshop on Geothermal Reservoir Engineering, Stanford, CA, Jan 22-Jan 24, p. 187-194.

McCluskey, S.C., Bjornstad, S.C., Hager, B.H., King, R.W., Meade, B.J., Miller, M.M., Monastero, F.C., and Souter, B.J. (2001), Present day kinematics of the Eastern California Shear Zone from a geodetically constrained block model. *Geophys. Res. Letters*, **28**(17), 3369-3372.

Monastero, F.C., Katzenstein, A.M., Miller, S.J., Unruh, J.R., Adams, M.C. and Richards-Dinger, K. (2005), The Coso geothermal field: A nascent metamorphic core complex. *GSA Bull.*, **177**(11/12), 1534-1553.

Moore, J., Norman, D., and Adams, M. (2004), Thermal and chemical history of the Eastern Coso geothermal field. Report to the Navy Geothermal Program Office. Report N68936-01-0095. 71 p.

Moos, D. and Zoback, M.D., (1990), "Utilization of observations of well bore failure to constrain the orientation and magnitude of crustal stresses: Application to continental, deep sea drilling project, and ocean drilling program boreholes," *J. Geophys. Res.*, **1000**(B), 12791-12811.

Peska, P. and Zoback, M. D. (1995) Observations of borehole breakouts and tensile wall fractures in deviated boreholes: A technique to constrain in situ stress and rock strength. *J. Geophys. Res*., **100**, 12791-12811.

Roquemore, G. 1981. Active Faults and Associated Tectonic Stress in the Coso Range, California. Naval Weapons Center, China Lake, California 93555, China Lake, CA, 101.

Roquemore, G. 1984. Structure, tectonics, and stress field of the Coso Range, Inyo County, California. *J. Geophys. Res.*, **85**(B5), 2434-2440.

Sheridan, J., Kovac, K.M., Rose, P. E., Barton, C. A., McCulloch, J., Berard, B., Moore, J. N., Petty, S. and Spielman, P. (2003), In situ stress, fracture and fluid flow analysis-East Flank of the Coso geothermal field. Twenty-eighth Workshop on Geothermal Reservoir Engineering, Stanford University, Stanford, California, January 27-29, SGP-TR-173, 16 p.

Sheridan, J. and Hickman, S., (2004), In situ stress, fracture and fluid flow analyses in well 38C-9: An enhanced geothermal system in the Coso geothermal field, Twenty-ninth Workshop on Geothermal Reservoir Engineering, Stanford University, Stanford, California, January 26-28, SGP-TR-175, 8 pp.

TerraTek. (2004), Physical and mechanical properties characterization of two granitic rocks, Coso EGS Project, TerraTek Inc., *Technical Report TR04-400872*, Salt Lake City, UT, 71 p.

Townend, J., and Zoback, M.D. (2004) How faulting keeps the crust strong. *Geology*, **28**, 399-402.

Unruh, J.R., Hauksson, E., Monastero, F.C., Twiss, R.J., and Lewis, J.C. (2002) Seismotectonics of the Coso Range—Indian Wells Valley region, California: Transtensional deformation along the southeastern margin of the Sierran microplate, in: Glazner, A.F., Walker, J.D., and Bartley, J.M., (eds), Geological evolution of the Mojave Desert and Southwestern Basin and Range: Boulder, CO, *GSA Mem.*, **195**, 227-294.

Whitmarsh, R.S. (1998), Geologic map of the Coso Range: *Geological Society of America on-line map, doi: 10.1130/1998-whitmarsh-coso*.

Wicks, C.W., Thatcher, W., Monastero, F.C., and Hasting, M.A., (2001), "Steady-state deformation of the Coso Range, East-Central California, inferred from satellite radar interferometry," *J. Geophys. Res.*, **106(B7)**, 13769-13780.

Unruh, J.R., and Streig, A.R. (2004), Mapping and characterization of neotectonic structures in a releasing stepover, northern Coso Range, easter California: Final technical report submitted to the U.S. Navy Geothermal Program Office, China Lake Naval Air Warfare Center, Contract N68936-02-C-0208, 46 p.

Zoback, M. D. Barton, C., Brudy, M., Castillo, D., Finkbeiner, T., Groolimund, B., Moos, D., Peska, P., Ward, C., and Wiprut, D. (2003) Determination of stress orientation and magnitude in deep wells. *Int. J. Rock Mehc. Min. Sci Geomech. Abstr.*,**40**, 1049-1076.